INDUSTRIAL X-RAY TOMOGRAPHY AS A TOOL FOR SHAPE AND INTEGRITY CONTROL OF SRF CAVITIES*

H.-W. Glock[†], J. Knobloch[1], A. Neumann, A. Velez-Saiz[2]

HZB für Materialien und Energie, Berlin, Germany

[1]also at University of Siegen, Siegen, Germany

[2]also at Technical University Dortmund, Dortmund, Germany

Abstract

Industrial X-ray tomography offers the possibility to capture the entire inner and outer shape of a superconducting radio frequency (SRF) cavity, providing also insights in weld quality and material defects. As a non-contact method this is especially attractive to investigate shape properties of fully processed and closed cavities. A drawback is the inherently strong X-ray damping of niobium, which causes the demand for intense hard X-rays, typically beyond the capabilities of dc-X-ray-tubes. This also limits the accuracy of material borders found by the tomographic inversion. To illustrate both capabilities and limitations, results of X-ray tomography investigations using three different cavities are reported, also describing the fundamental parameters and the hard- and software demands of the technology. We also discuss the non-trivial transferring of tomography data into RF simulation tools.

INTRODUCTION

The extraordinary small line width of SRF cavity resonators makes it desirable to provide best geometrical control of such cavities whilst the entire sequence of production, preparation and installation. Furthermore such cavities are costly and delicate devices, which require best practiced quality control. Third they demand for highest cleanliness and should kept hermetically closed as far as possible. It is the aim of this paper to estimate the potential of industrial X-ray tomography (cf. Figs. 1 and 2) to serve as a tool for cavity shape and integrity control, since it matured in various fields – a very early reference is found in [1], a recent summary in [2] – as a non-destructive, non-tactile, highly permissive and accurate method. The term "industrial" shall be understood both as technical distinction from medical X-ray tomography, but also in the sense of a procurable service. In other words: Does it work and can we buy it?

The authors do not claim the priority being the first to apply X-ray tomography to a Niobium cavity, which to our best knowledge, was described in [3], there with a focus on surface defect analysis. Those experiments triggered our investigations applied to more and larger structures with higher wall thicknesses, also utilizing a significantly higher X-ray energy.

Figure 1: Gun1.1-cavity (1, [4]) placed in between a 300 keV X-ray tube (2) and a detector array (3) on a rotating (4) and lifting (5) table in a shielded cabinet with a lead glass window (6) at XRAY-LAB, Sachsenheim, Germany.
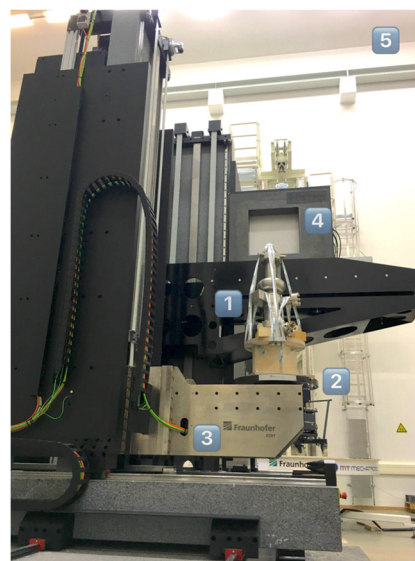

Figure 2: VSR-Single-Cell cavity (1, [5]) mounted on the rotating table (2) at the Fraunhofer-EZRT large scale X-ray tomography installation, Fürth, Germany [6]. The lifter (3) will move the cavity in the X-ray beam generated by a 9-MeV-accelerator-based source (not shown) in the height of the square X-ray array detector (4). For radiation protection the entire installation is housed in a bunker (5).

THOTEV07

It is beyond the scope of the paper to report progresses in either the technology of superconducting cavities nor in that of X-ray tomography. But it is the aim of this paper to demonstrate the linkage of both about which, to the best of authors' knowledge, no in-depth study is available. So it may serve as a basis for estimates about further applications of that method, which provides in an unprecedented manner control of the integrity and full inner shape of a cavity, even though it can remain hermetically closed during the measurement.

VERY BASICS OF X-RAY TOMOGRAPHY

Tomography (derived [7] „from Greek tomos: section, roll of papyrus, tome, from temnein: to cut") in general describes the revealing of the internal structures of material distributions by evaluating the measured interaction with certain radiation, passaging the material distribution – later on: the test object – on various paths.

In general this demands first for the ability of the radiation to transmit the entire test object without getting weakened too much not to be measurable afterwards. Nevertheless it is mandatory that the radiation interacts with the material intensively enough to provide a detectable effect. At third it is desirable to apply a very narrow radiation beam (of whichever radiation), as – somewhat simplified – no internal structure smaller than the width of the beam may be resolved. The measured effect on the transmitted radiation of a single beam is a single-valued result, integrating over the entire path through the test object. Its internal structure therefore only can revealed by combining many measurements, taken with different beam paths through the structure, such that any volume element contributes to the effect in several different paths.

Said that, it becomes a natural concept to understand the test object as constituted of a large, but limited number of small non-overlapping, but directly attaching volume parts, denoted as voxels, which are approximated as being of homogeneous property with respect to the interaction mechanism(s) with the radiation beams. Not necessarily, but most often those voxels are assumed to be of cubic shape and all of identical size.

The fundamental mathematical principle which states, that the number of unknowns must not exceed the number of equations, translates here to a limit for the number of voxels used to describe an arbitrarily structured test object given by the number of single measurements. It should be emphasized, that those voxels are a purely mathematical concept to approximate the volume structure of the test object, but they are no autonomous physical entities by themselves.

The fundamental concept described above may be realized with various kinds of matter-radiation interaction, but its certainly most prominent example is X-ray absorption tomography, originally developed for medical applications and granted with the 1979's Nobel prize in Physiology or Medicine [8]. The price acclamation originally reads: „for the development of computer assisted tomography", which indirectly highlights the need of sophisticated mathematics and significant computational demands to perform the deconvolution from measurable X-ray damping on certain beam paths to a voxel-individual specific X-ray absorption rate, which then indicates the kind of material in every single voxel. Both the underlying mathematics and algorithms are beyond the scope of this paper and will be accepted here as well understood and available in black-box instances. Readers interested in details may start with the key words "Radon transformation" and "Filtered back projection".

Industrial X-ray tomography, whilst sharing the same principles, is mainly distinct from medical applications by (much) higher X-ray energy and dose rates the test objects may be exposed to. (In other words: the „patients" are already dead.) On the other hand, materials – often metals – and samples with typically much stronger X-ray absorption than that of biological probes are to be tested.

X-Ray Intensity Decay

The kernel of X-ray absorption tomography is given by the direct local proportionality between radiation intensity I and its weakening dI along a short part dx of its propagation path:

$$dI(x) = -\mu I(x) dx \qquad (1)$$

The damping coefficient μ (dimension 1/length) depends heavily on the energy of the photons (see below) and on the material through which the radiation propagates. In fact it is the core task of the tomography process to determine the spatial distribution of μ in the test object in order to conclude about the material distribution. That implies that different materials with similar damping coefficients are hardly to distinct. For the special case of μ being constant in a certain range Eq. (1) is solved by an exponential intensity decay:

$$I(x) = I_0 e^{-\mu x} \qquad (2)$$

X-ray absorption tomography ignores the wave character of X-rays, making it applicable to fully incoherent radiation and large amorphous samples. Then all relevant interaction processes, as discussed below, affect just single atoms. So the evaluable material property reduces to the stoichiometric composition based on pure elements (e.g. in contrast to X-ray diffraction, which depends on crystal lattice properties), which makes it sensible to tabulate their density-normalized absorption coefficients μ/ρ (of dimension $length^2/mass$) as it is done in prominent collections like [9]. Absorption of any kind of chemically or otherwise composed material then easily is derived as a density-weighted sum.

X-Ray Interaction with Matter

Three fundamentally different interaction mechanisms of X-rays with matter are relevant here (cf. Fig. 3) and shall

be discussed in a very superficial manner: (i) photoelectric absorption of photons with release of an electron out of an atomic shell; (ii) inelastic, so-called Compton scattering of photons at electrons, resulting in a photon travelling further with reduced energy and altered direction plus a moving electron; (iii) production of an electron-positron-pair with annihilation of the photon.
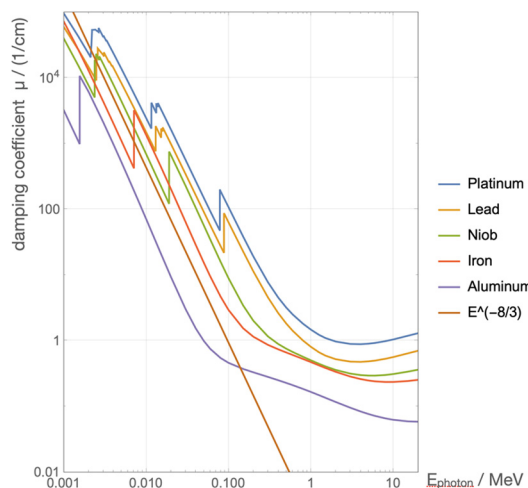

Figure 3: Spatial photon intensity damping coefficients of metals using computed data provided in [9] using known densities. Up to about 100 keV … 250 keV photoelectric absorption with element-characteristic edges dominates, while a slight damping increase caused by the onset of pair production is observed above ~ 5 MeV. Least damping is found in between both regimes where Compton-scattering is the most likely process.

Pair production obviously cannot happen if the incident photon arrives with less than the rest energy of the electron-positron pair, which is $2 \cdot 511$ keV. It gets relevance above some 5…10 MeV photon energy. For higher photon energies its likeliness keeps slowly growing, so there is no gain in mass-specific transmissibility by increasing the photon's initial energy significantly beyond 10 MeV.

The probability of *photoelectric absorption* of the photon in general decreases rapidly with increasing energy (an empirical fit of $E^{-(8/3)}$ gives a good approximation), but is raised with element-specific sawtooth-like patterns of threshold energies at the various ionization energies of the atomic shells. For lower atomic numbers this regime is relevant for photon energies up to ~ 100 keV; materials of higher atomic number, i.e. with more and stronger bound inner electrons – this includes niobium – show dominant photoelectric absorption up to ~ 250 keV.

The most advantageous photon energy range in order to transmit a thick and/or strongly absorbing sample (as it is often intended if X-ray tomography is industrially applied) lies in between those two previously mentioned regimes, i.e. in the energy range ~ 250 keV to ~ 5 MeV. Then *incoherent*, so called *Compton scattering* is the dominant process. It is the only one of the three which does not end the photon's journey by full absorption. Instead it

experience an energy loss and a change of direction, whilst the electron is released from the atomic shell and balances energy and momentum preservation. The probability of such a scattering is described in the famous Klein-Nishina-Formula [10], derived for an electron in an unbound state (corrections apply for bound electrons, which do not cause essential changes). It basically results (cf. Fig. 4) in (i) a scattering probability getting the lower, the higher the photon's energy, (ii) a strong preference for MeV-photons to keep their direction within small angular deviations, and (iii) low-energy-photons being prone to strong deflections, backscattering almost as likely as passing by.
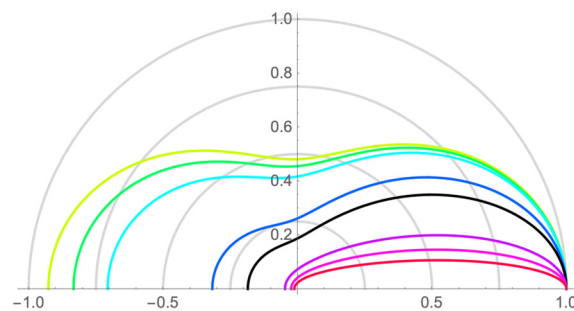

Figure 4: Relative (with a common scale for all curves) direction-dependend Compton scattering probability for photon energies of 10 keV (light green), 25 keV, 51 keV, 250 keV, 511 keV (black), 2.50 MeV, 5.11 MeV, 10 MeV (red) following the Klein-Nishina formula for the differential cross section (cf. [10], p. 404).

The total Compton scattering probability obviously is directly proportional to the electron density, which itself increases with the number of atoms per volume and their atomic number. Compton scattering in general may happen at any photon energy, but its contribution gets negligible both in the low energy range, where photoelectric absorption strongly dominates and in the high energy range, where pair production gets much more likely. The high probability of significant angular deviation caused by Compton scattering of low and medium energies is unwanted in tomographic measurements as it broadens the beam, thus violating the assumption of a straight line between source and each individual detector element.

Without discussing any further details it should be mentioned that also secondary effects happen due to electron capture after the ionization, electron-positron annihilation after pair production and bremsstrahlung generation by moving electron or positrons. All these mechanisms generate secondary photons in the material, which themselves may leave the sample or experience further interactions. The combination of Compton scattering with any other effect is also possible. Numerical simulations of large ensembles of starting photons nowadays allow to analyse the statistics of such complicated cascades in realistic geometrical and spectral conditions (e.g. [11] including comparison with measured results, [12] comparing two well established programs, revealing quite significant differences). It's complicated.

TOMOGRAPHY SETUP, KEY PARAMETERS AND WORKFLOW

Following the very general remarks above, three hardware elements are essential to perform X-ray tomography (cf. Fig. 5). Obviously that are a radiation source, a multi-element X-ray intensity detector and a mean to rotate (in small angular steps) the test object through the curtain of X-ray beams between the source and each detector element. It is the rotation of the test object, that generates in every angular step a new combination of voxels in every of the beam paths, adding up to integral X-ray absorption rates, which are detected as intensity values in every single detector element.
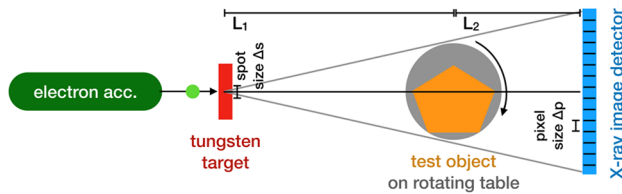

Figure 5: Main components and quantities of a tomography setup as explained in the text. Please note, that the two-dimensionality is an inherent property of the tomography approach; not just a schematic simplification used in the viewgraph (picture first shown in [13]).

Detector Arrays

In principle, it would be possible to sample each beam path one after another, e.g. using a single moving detector. In practice this is hardly feasible in view of the time needed to make such a movement, which then would need to be repeated for every single angular step. Therefore array detectors are an essential technique to effectively perform tomography captures. Such detectors are commonly based on the combination of a szintillating layer (or a layer of separated segments), converting the incident radiation into photons of the visible spectral range combined with CCD/CMOS sensor arrays. A variety of aspects – pitch size, spectral conversion efficiency, bandwidth, noise level etc. – need attention to tailor such detectors, which is beyond the scope of this paper. A detailed overview covering various detection principles is found e.g. in [14].

In tomographic applications one has to distinct line array detectors, providing data for one singular cut-plane through the test object, and surface detector arrays, which intrinsically provide data for many vertically (i.e.: parallel to the rotation axis) stacked cut-planes through the object in one shot. Again it is possible – though very time consuming – to collect the same data out of a single surface array capture or by many captures of vertically shifted line detector. The tomographic deconvolution happens individually for each cut-plane (here excluding higher-level corrections e.g. for inter-plane radiation scattering), which further gives the freedom to study test objects with a large extension in one dimension by combining many piecewise captured sections, provided there is a

mechanical mean to shift the test object along the axis of rotation.

A simple, whilst meaningful aspect of tomographic inspections is the limitation of the object size transversal to the axis of rotation, which is determined by the coverage of beam paths between source and the outermost elements of the detector array. If this features N_d detector elements in a row with a total width $N_d \cdot \Delta p$, the biggest measurable diameter D_{obj} is:

$$D_{obj} < \frac{L_1}{L_1 + L_2} \cdot N_d \cdot \Delta p \qquad (3)$$

State-of-the-art surface arrays come with more than 2000 x 2000 single detector elements and available sizes up to $(0.5 \text{ m})^2$, whilst large line arrays can be combined out of smaller arrays to up to $\sim 10^4$ single detectors and lengths of a few meters [6]. Such special set-ups impressively demonstrate the technique's abilities in scanning test objects as large as e.g. complete passenger cars, but with the price of extremely long scanning times.

Applied to cavities, surface array detectors will be given the preference. Then, following equation (3), the biggest accessible diameter is about 90% of the array size, i.e. 450 mm. This is sufficient for cavities with fundamental frequencies roughly above 1 GHz, but may cut off long radial extension.

X-Ray Sources

DC-voltage driven evacuated, so called X-ray tubes are the most common devices for X-ray generation since Röntgen's discovery and are still matter of technological development [15]. Those use a current of electrons emitted from a heated cathode and accelerated by a DC-voltage towards hitting an anode made out of a dense material (mostly tungsten) in order to produce an overlay of both bremsstrahlung and characteristic X-ray emission. The latter stems from the recombination of ions, themselves generated by ionizations directly through electronic impact or photoelectric absorption of photons. Whilst the characteristic part of the emitted X-rays has energies determined by the anode's material, the upper limit of the widely spread bremsstrahlung spectrum can be shifted towards higher energies by increasing the accelerating voltage.

The fast decay of photoelectric absorption (cf. Fig. 3) fostered the use of increasing voltages in X-ray tubes intended for applications which need high penetration. Those now are commercially available with accelerating voltages up to 600 kV [16], which sounds rather superior to the more common "classes" of 150 kV-, 225 kV-, 300 kV- or 450 kV-tubes. Nevertheless the progress is much lessened in view of the bremsstrahlung spectrum, which contains only a minor fraction (actual numbers depend on the anode's geometry) of photons with energies close to the initial kinetic energy of the electrons (cf. [17], Fig. 7 for various energies, also [11], Fig. 2 for a 450 kV tube). Therefore one will achieve improved transmission

when changing from 300 kV to 600 kV, but far less than intuitively expected from the absorption coefficient (cf. Fig. 3) at the electron's kinetic energy value

The need to reach significantly higher mean photon energies in order to raise transmission in samples with large material thickness and/or strong absorption led to the application of RF-based accelerators in order to provide electron energies of 5 … 10 MeV in tomographic systems (e.g. [18] as early as 1993, using a 12-MeV-accelerator, [19] including a simulated photon spectrum, [20], [21]). The change of technology is needed because of breakthrough limitations, which make such high accelerating DC voltages not feasible.

Mechanics and Shielding

Dealing with spatial accuracy in the order of (see below) 0.2 mm demands for the same degree of geometric precision in the mechanics of all relevant components, even though they may be extended over several meters and of large-scale weights. That also affects the demand of thermal stability in a sub-degree range during the capturing process, which takes in the order of 10…30 minutes.

Finally an appropriate shielding of the setup is needed for safety reasons. Since parasitic X-ray scattering in the shielding may significantly contribute to the background detector signal, causing artefacts and reducing the signal-to-noise ratio, a large distance of the shielding is strongly desirable.

Data and Work Flow

The data and work flow as used here are illustrated in Fig. 6. All scanning and tomographic reconstruction were done by XRAY-LAB, Sachsenheim, Germany and Fraunhofer Institute for Integrated Circuits IIS, Development Center X-ray Technology EZRT, Fürth, Germany, using their installations and proprietary reconstruction software. This resulted in 3-dimensional arrays of voxel absorption data, saved as canonically ordered lists of 2-byte grayscale values, denoted as ".rek" files. Those files are uncompressed and of a size of $\sim 2 \cdot (2000)^3$ Bytes, which makes them rather unhandy. VolumeGraphics© [22] and GOM-Inspect© [23] were used for display, material surface determination (which is discussed below), dimensional control, comparison with construction data and surface export. the latter using the widely used ".stl" format, which apply triangle surface elements as surface approximation. The output of both programs unfortunately is not the triangulation of a single watertight surface. Instead the programs attempt also to represent spurious volumes which may locally exceed the threshold value chosen to define the material border, especially if this boundary zone is diffuse because of an unclear tomographic reconstruction. Even worse also many non-closed surfaces are found in the ".stl" files (cf. [13], Fig. 4). This renders the ".stl"-files incompatible with the import capabilities of field solvers like CSTStudio© [24]. A conversion into a volume model of the cavity wall using the smoothing, error correction and export capabilities of

Geomagic Design X [25] was the only cure found to deal with that issue. This program tries to identify regular and smooth surfaces in point clouds, which then are expressed as B-splines. Those are valid primitives of the STEP format, which is commonly understood. Nevertheless this process is not fail safe. It gets the more reliable the less noise is contained in the initial point cloud. This directly correlates to a clear result of the tomographic inversion, which in turn only is given if damping is not too strong
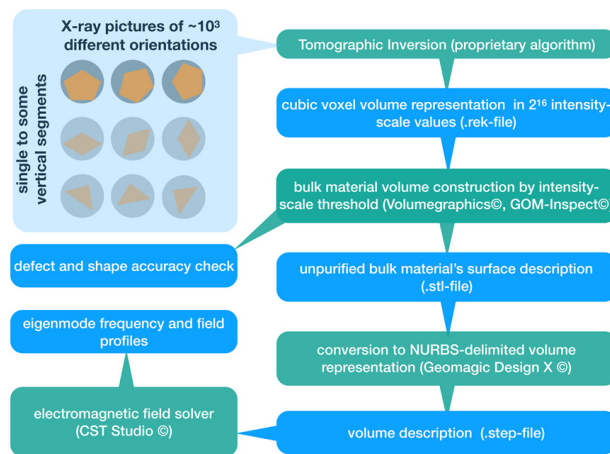

Figure 6: Data and workflow (picture first shown in [13])

TOMOGRAPHY RESOLUTION LIMITS

The spatial resolution limits of X-ray tomography are twofold: First there is only a limited information contained in the total number of measurements $N_a \cdot N_d$ to which the number of voxels in a single cut plane is restricted. Herein N_a is the number of angular steps, N_d number of beam paths sampled for each angular orientation, typically the number of detector elements. (The argument is somewhat simplified: It is possible to assign smaller, i.e. more voxels, but not to raise the spatial bandwidth of the result.) At a first glance one would assume that even a very low number of separable beam paths, i.e the use of rather wide beams, could be compensated just by increasing the number of angular steps. This concept obviously breaks down once two neighbouring orientations get that close that both measurements cover the contribution of – in extreme – the identical voxel set. It fails even earlier once the result of two adjacent angular samplings gets that close that they are distinct only by a fraction comparable to the experimental noise of the intensity detection, which would make the tomographic deconvolution fully ambiguous.

That leads to the second resolution limit, as it demands for radiation beam paths as narrow as possible. This effective beam path width Δd is for obvious geometric reasons both determined by the width of the X-ray source spot Δs and the width of the detector elements Δp. From geometric considerations Δd can be derived [26] as:

$$\Delta d = \frac{\sqrt{[L_2 \Delta s]^2 + [L_1 \Delta p]^2}}{L_1 + L_2} \qquad (4)$$

Evaluating this for a DC-X-ray gun set-up as used in this study ($L_1 + L_2 = 2500$ mm, $L_1 = 1786$ mm, $\Delta s \sim 0.5$ mm, $\Delta p = 0.2$ mm) results in $\Delta d \sim 0.20$ mm. The high relevance of a narrow radiation spot – for so-called micro- and nano-tomography with its purpose for highest spatial resolution being the key figure-of-merit – is illustrated in Fig. 7. There its size Δs is varied according Eq. (4) (using the aforementioned parameters) from a singular point to 1 mm diameter, causing an increase of the size of least resolvable details in this specific set-up from 143 µm to 319 µm.
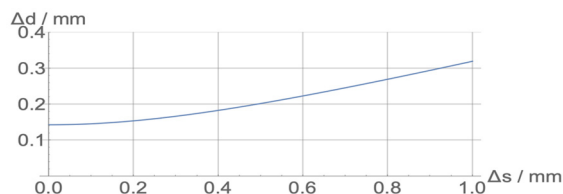

Figure 7: Spatial resolution limit depending on X-ray spot size following Eq. (4) and parameters given above.

TOMOGRAPHY OF SRF CAVITIES IN PRACTICE

This work is based on the tomography tests done at XRAY-LAB with a 300 keV DC-tube setup (cf. Fig. 1) and at Fraunhofer-EZRT, where both a 587 keV DC-tube setup and the large accelerator (Siemens SILAC 9 MeV) driven machinery was used (cf. Fig. 2). Details about the three test objects – a "generic" 1.3 GHz single cell (SC-) cavity, the 1.3 GHz, 1.4-cell Gun 1.1-cavity and the 1.5 GHz VSR-1-cell-prototype (VSR1C-) cavity – were already explained in [4], [5] and [13]. Here new evaluations of those data are shown.

Surface Reconstruction from Damping Thresholds

Pictures of cross sections through the voxel tomographically reconstructed sets typically display those as grayscale with the convention of zero damping (the aerial background) shown in black, strongest absorption in white. A human spectator is able to interpret such visualizations quite intuitively and often will be able to identify features like voids or cracks, which is one of the key merits of tomography.

This nevertheless is not sufficient to derive quantitatively material dimensions, which essentially demands for the determination of material surface locations. Such are defined by the choice of a least computed damping (i.e. grayscale) value, above which the voxel is assigned to a certain material; all damping values below the (lowest) material threshold understood as empty. Obviously such an assignment is hindered by the wide variation of absorption values, which are computed for a certain material (cf. the broad spectrum shown in Fig. 8). They are first caused by the wide variations of material thicknesses, second since X-ray absorption is blurred by any kind of non-straight energy propagation from source to detector (as discussed via Compton scattering, diffuse radiation from recombination or annihilation processes,

bremsstrahlung generation from moving electrons, radiation from ambient scatterers etc.). Third the tomographic inversion also introduces weighting variations (e.g. between central and peripheral areas, in comparison of slices with strongly differing integral damping, by boundary artefacts etc.). Filtering and correction algorithms are in use, but their discussion is beyond our competence.
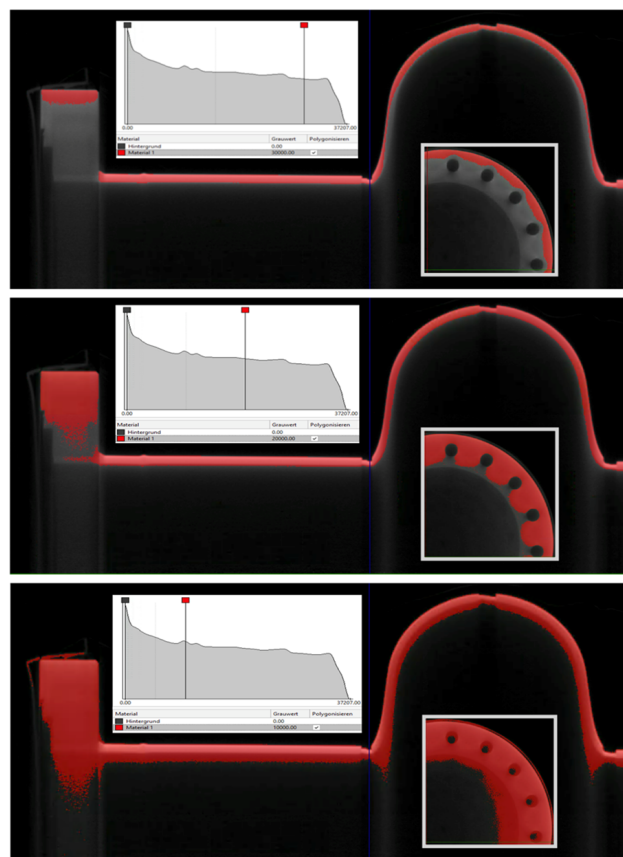

Figure 8: Parts of cut planes through the voxel set of the SC-cavity (longitudinal, upper half) and a sector of its stainless steel flange (inset). Red colored overlay highlights local absorption values above three differently chosen threshold values as indicated in the histogram insets (which accounts the full volume dataset). The choice of the threshold value directly affects any kind of surface determination or thickness measurements. Pictures generated with [23].

So a priori knowledge is inevitable for the interpretation of tomography voxel data and especially the appropriate choice of threshold values as input for surface determinations: Comparison with externally visible features, calibration with accessible dimensions (e.g. of standards added to the sample), (non)conformity within several items of a series, comparison within the different regions of a test device expected with similar appearance, educated knowledge about typical artefacts and difficult radiation conditions merge to a decision about the validity of a tomographic assessment.

Noisy Surface Detection

Figure 9, which shows the tomographic reconstruction of the SC-cavity captured with the Linac setup both in a 3D-cut representation of the inner surface and a cross section of the absorption density (left), give the impression of a rough surface within a certain radial zone. This zone seem to be quite clearly separated both from the strong inner bending towards the beam pipe and the outer bending towards the cell equator. The visual inspection in contrast revealed no significantly varying surface roughness, whilst the reconstructed absorption density is clearly reduced in the respective zone. This is attributed to the small angle between the radiation path and the niobium sheet there, leading to a strong overall damping and giving a poor contrast available to detect the material surface, which therefore appears quite noisy. Such effects also were observed on outer surfaces as shown in Fig. 10.
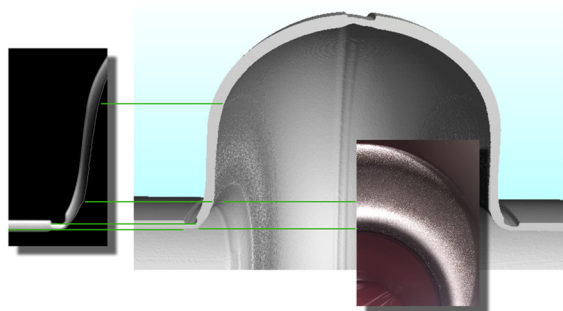

Figure 9: Surface reconstruction and absorption density (left) of the SC-cavity give the impression of enhanced surface roughness in the steep flank part. The photo of the corresponding area (courtesy S. Nottrott, Fraunhofer-EZRT) reveals this as an artefact.
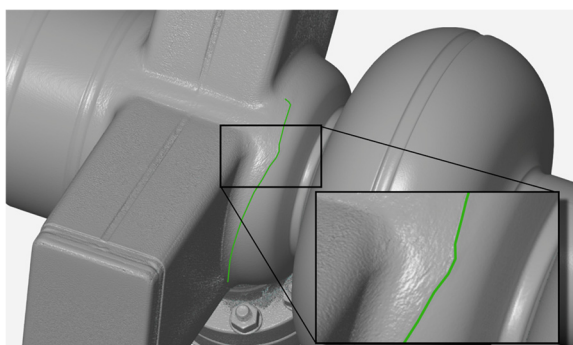

Figure 10: The green line marks border of a shadow zone caused by additional damping due to the waveguide extensions of the VSR1C-cavity. Smooth surface reconstruction outside, i.e. right to the shadow. The cavity was mounted slightly tilted in order to avoid too strong damping in the flat waveguide surfaces.

Benefits of High-Energy X-Rays

The Gun 1.1-cavity was scanned with X-rays both from 300 keV and 587 keV DC tubes and also with the 9 MeV Linac setup. This gives the rare opportunity to compare those directly, cf. Fig. 11. Each threshold value was manually adjusted to give the best overall reconstruction. Clearly the 300 keV results are fully insufficient, whilst those captured with 587 keV deliver good outer but mostly poor inner contours, also lacking most of the cavity's complicated inner structure. The X-rays from the 9 MeV electrons give a much clearer resolution also from the interior parts, even though the narrow cathode channel is kept erroneously closed and still noise appears in the rightmost flange.
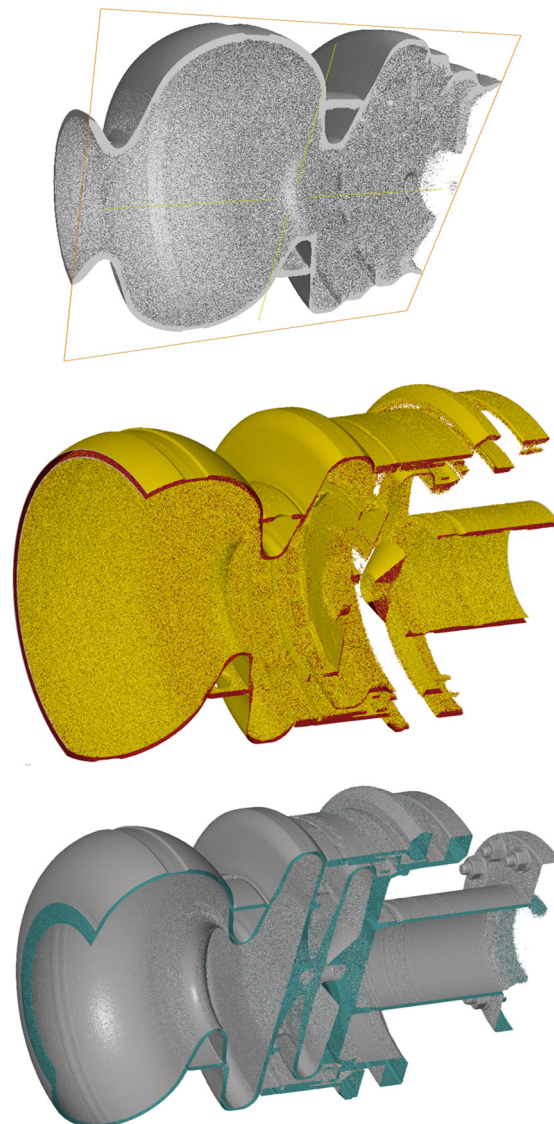

Fig. 11: Cross sections of tomographic reconstructions of the Gun 1.1-cavity with 300 keV (top), 587 keV (middle) and 9 MeV electrons (bottom) used for X-ray generation.

CONCLUSION

Industrial X-ray tomography for SRF cavities? First it clearly is not industrial in the sense of a routinely available commercial application, since niobium is an unfavourable material because of its strong absorption in the photon energy range below 300 keV, which demands for one of the rare installations providing highest electron energies

available from DC-driven X-ray tubes or preferably a Linac-driven source. Second the cavity diameter including extensions needs to be kept limited to ~ 400 mm to fit with available surface detectors. Third common elliptical cavity shapes are prone to strongly differing integral absorptions leading to difficult surface determination in the flank regions which are almost parallel to the X-ray beam. There the geometrical accuracy, which typically can reach ~ 0.25 mm, is significantly worse.

SRF technology – on the other hand – is demanding in almost any aspect. Once this is accepted, industrial – in its pure technical sense – X-ray tomography gives an unprecedented mean both to integrally capture the cavity's geometry under hermetically closed conditions (and even enclosed in a tank) and to indicate material and manufacturing imperfections.

Non-destructive testing of any kind relies to a big extend on experience specific to the method and to the samples. In the case of X-ray tomography for SRF cavities, we just started to collect it.

ACKNOWLEDGEMENTS

REFERENCES

[1] S. Izumi *et al.*, "High Energy X-ray Computed Tomography for Industrial applications", *IEEE Trans. Nucl. Sci.,* vol. 40, pp. 158–161, 1993. doi: 10.1109/23.212333

[2] L. De Chiffre *et al*., "Industrial applications of computed tomography", *CIRP Annals - Manufacturing Technology*, vol. 63, pp. 655–677, 2014. doi: 10.1016/j.cirp.2014.05.011

[3] M. Bertucci et al., "Test, diagnostics and computed tomographic inspection of a large grain 3.9 GHz prototype cavity", in *Proc. 8th Int. Particle Accelerator Conf. (IPAC'17)*, Copenhagen, Denmark, May 2017, pp. 1011-1014. doi 10.18429/JACoW-IPAC2017-MOPVA062

[4] H.-W. Glock, J. Knobloch, A. Neumann, Y. Tamashevich, "Preparation and Testing of the BERLinPro Gun1.1 cavity", in *Proc. 9th Int. Particle Accelerator Conf. (IPAC'18)*, Vancouver, Canada, doi:10.18429/JACoW-IPAC2018-THPMF032

[5] A.Velez et al., "The SRF Module Developments for BESSY VSR", in *Proc. 8th Int. Particle Accelerator Conf. (IPAC'17)*, Copenhagen, Denmark, May 2017, pp. 986-989, doi:10.18429/JACoW-IPAC2017-MOPVA053

[6] M. Salamon *et al.*, "High Energy X-Ray Imaging for Application in Aerospace Industry", 4th Int. Symp. On NDT in Aerospace 2012, Tu.4.A.2

[7] "Tomography." Merriam-Webster.com Dictionary, Merriam-Webster, Accessed 27 Oct. 2020. https://www.merriam-webster.com/dictionary/tomography

[8] The Nobel Prize in Physiology or Medicine 1979, https://www.nobelprize.org/prizes/medicine/1979/summary/

[9] J. H. Hubbell, S. M. Seltzer, "X-Ray Mass Attenuation Coefficients" last updated July 2004. doi: 10.18434/T4D01F

[10] Y. Yazaki, "How the Klein–Nishina formula was derived: Based on the Sangokan Nishina Source Materials," Proc. Jpn. Acad., Ser. B, vol. 93, pp. 399-421, 2017. doi: 10.2183/pjab.93.025

[11] A. Miceli *et al.*, "Monte Carlo simulations of a high-resolution X-ray CT system for industrial applications", *Nucl. Instrum. Methods Phys. Res. A*, vol. 583, pp. 313–323, 2007. doi:10.1016/j.nima.2007.09.012

[12] M. Kiunke et al., "ROSI and GEANT4 - A comparison in the context of high energy X-ray physics", *Nucl. Instrum. Methods Physics Research B*, vol. 377, pp. 50-58, 2016. doi: 10.1016/j.nimb.2016.04.029

[13] H.-W. Glock, "Operational Experiences with X-ray Tomography for SRF Cavity Shape and Surface Control", in *Proc. 10th Int. Particle Conf. (IPAC'19)*, Melbourne, Australia, May 2019, pp. 2838-2841, doi:10.18429/JACoW-IPAC2019-WEPRB017

[14] J. G. Rocha1 & S. Lanceros-Mendez, "Review on X-ray Detectors Based on Scintillators and CMOS Technology", *Recent Patents on Electrical Engineering 2011*, vol. 4, 2001. doi:10.2174/1874476111104010016

[15] R. Behling, "X-ray sources: 125 years of developments of this intriguing technology", *Physica Medica, v*ol. 79, pp. 162–187, 2020. doi: 10.1016/j.ejmp.2020.07.021

[16] M. Krumm *et al.,* "Comparative Study on the Benefits of 600 kV Computed Tomography Systems and its application in aerospace industry", iCT Conference 2014. https://www.ndt.net/article/ctc2014/papers/411.pdf

[17] A. Hernandez & J. Boone, "Tungsten anode spectral model using interpolating cubic splines: Unfiltered x-ray spectra from 20 kV to 640 kV", *Med. Phys.*, vol. 41, 2014. doi:10.1118/1.4866216

[18] S. Izumi, "High Energy X-ray Computed Tomography for Industrial Applications," *IEEE Trans. Nucl. Sc.,* vol. 40, pp. 158-161, 1993. doi:10.1109/23.211333

[19] L. Auditore *et al*., "Design of a 5 MeV electron linac based X-ray source", *Nucl. Instr. Meth. Phys. Res. Sec. B*, vol. 240, pp. 913-922, 2005. doi:10.1016/j.nimb.2005.06.205

[20] L. Auditore, "A Compact 5 MeV, S-Band, Electron Linac Based X-Ray Tomography System", in *Proc. 10h European Particle Accelerator Conf. (EPAC'06),* Edinburgh, UK, 2006, paper WEPCH187, pp. 2370-2372.

[21] A. Flisch et al., "High energy CT with portable 6 MeV linear accelerator", iCT Conference 2014, https://www.ndt.net/article/ctc2014/papers/239.pdf

[22] VolumeGraphics VGStudio 3.2, Volume Graphics GmbH, Speyerer Straße 4 – 6, 69115 Heidelberg, Germany

[23] GOMInspect v2018, GOM GmbH, 38122 Braunschweig, Germany

[24] Simulia CST Studio Suite Vers. 2019.05, Dassault Systems Deutschland GmbH

[25] Geomagic Design X Vers. 3.2, 3D Systems Corporation, Rock Hill, SC 29730, USA

[26] American National Standard, "Standard Guide for Computed Tomography (CT) Imaging, E1441–97", ASTM, West Conshohocken, PA 19428-2959, USA, pp. 15-16